



This is a repository copy of *Microstructural evolution of Mn-based maraging steels and their influences on mechanical properties*.

White Rose Research Online URL for this paper:

<http://eprints.whiterose.ac.uk/104180/>

Version: Accepted Version

Article:

Qian, F., Sharp, J. and Rainforth, W.M. orcid.org/0000-0003-3898-0318 (2016)
Microstructural evolution of Mn-based maraging steels and their influences on mechanical properties. *Materials Science and Engineering A*, 674. pp. 286-298. ISSN 0921-5093

<https://doi.org/10.1016/j.msea.2016.08.006>

Article available under the terms of the CC-BY-NC-ND licence
(<https://creativecommons.org/licenses/by-nc-nd/4.0/>)

Reuse

This article is distributed under the terms of the Creative Commons Attribution-NonCommercial-NoDerivs (CC BY-NC-ND) licence. This licence only allows you to download this work and share it with others as long as you credit the authors, but you can't change the article in any way or use it commercially. More information and the full terms of the licence here: <https://creativecommons.org/licenses/>

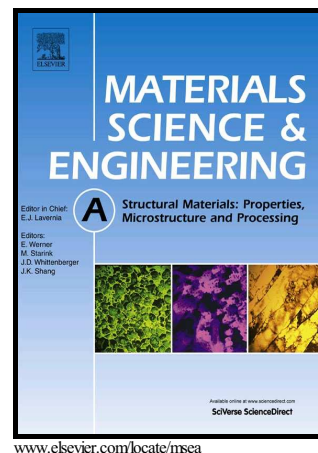
Takedown

If you consider content in White Rose Research Online to be in breach of UK law, please notify us by emailing eprints@whiterose.ac.uk including the URL of the record and the reason for the withdrawal request.

Author's Accepted Manuscript

Microstructural evolution of Mn-based maraging steels and their influences on mechanical properties

Feng Qian, Joanne Sharp, W. Mark Rainforth



PII: S0921-5093(16)30906-6

DOI: <http://dx.doi.org/10.1016/j.msea.2016.08.006>

Reference: MSA33964

To appear in: *Materials Science & Engineering A*

Received date: 13 June 2016

Revised date: 1 August 2016

Accepted date: 2 August 2016

Cite this article as: Feng Qian, Joanne Sharp and W. Mark Rainforth
Microstructural evolution of Mn-based maraging steels and their influences on mechanical properties, *Materials Science & Engineering A*
<http://dx.doi.org/10.1016/j.msea.2016.08.006>

This is a PDF file of an unedited manuscript that has been accepted for publication. As a service to our customers we are providing this early version of the manuscript. The manuscript will undergo copyediting, typesetting, and review of the resulting galley proof before it is published in its final citable form. Please note that during the production process errors may be discovered which could affect the content, and all legal disclaimers that apply to the journal pertain

Microstructural evolution of Mn-based maraging steels and their influences on mechanical properties

Feng Qian, Joanne Sharp, W. Mark Rainforth

Department of Materials Science and Engineering, University of Sheffield, Sheffield, S1 3JD, UK

Abstract

The microstructural evolution in a set of Mn-based maraging steels (7-12 wt.% Mn) when aged at 460-500 °C for various durations up to 10080 min and the influences on mechanical properties are systematically investigated. The improved yield strength of peak-aged samples is attributed to the formation of Ni₂TiAl precipitates and the precipitation strengthening is governed by Orowan mechanism. Segregation of Mn at grain boundaries in the initial aging stage resulted in severe intergranular brittleness. During further aging, accumulated Mn segregation leading to the formation of ductile lath-like reverted austenite removed the embrittlement and significantly improved the ductility. In the overaged condition, the steady work hardening after yielding compensates the loss of yield strength resulting from the coarsening of precipitates and softening of α' -martensite matrix. There was only limited evidence of the TRIP effect in the reverted austenite, indicating that work hardening was associated with other deformation mechanisms. Increasing the aging temperature or the Mn content of alloy that promotes austenite reversion was demonstrated to accelerate the improvement of ductility.

Keywords: maraging steels, Ni₂TiAl, precipitation strengthening, austenite reversion, transmission electron microscopy; strengthening mechanism

1 Introduction

Steels possessing a good mechanical balance (tensile strength \times elongation) are of great importance to their applications. Specifically in the automotive industry, they are regarded as the future key materials for light-weight strategies and related fuel and car emissions savings [1][2][3]. The huge commercial demand has driven both industry and academia to make great progress in developing advanced high-strength steels (AHSS). Transformation-induced plasticity (TRIP) steels are a representative family of AHSS, which consist of a multiphase

microstructure via sophisticated alloying design and processing paths. The ultimate tensile strength (UTS) of commercial TRIP steels has been improved over the years and is now approaching the GPa-level, but the total elongation (TE) tends to deteriorate to below 15% when the tensile strength exceeds 800 MPa [2]. Recently, low-carbon manganese TRIP steels (5-12% Mn) have been extensively studied as an alternative TRIP steel grade with equivalent (or better) mechanical properties but improved weldability and lower production costs [1][2][4][5][6][7][8][9][10][11][12][13][14]. In contrast to conventional TRIP steels, these Mn TRIP steels generally possess dual-phase microstructures comprised of different proportions of ferrite and retained austenite (20-40%) [8]. Therefore, the processing is simplified to quenching followed by an intercritical annealing (cold rolling was conducted after quenching in some cases [5][8][13]). For laboratory based materials, the UTS of Mn TRIP steels can reach approximately 1-1.2 GPa with an elongation of 20-40% [5][7][8][9]. Shi et al. [14] reported a series of Mn steels exhibiting a UTS up to 1.4 GPa with a tensile elongation of 31%.

Driven by the motivation to reduce the production costs of maraging steels (a group of precipitation-strengthened AHSS by intermetallic compound instead of carbide), the strategy of substituting expensive alloying elements such as cobalt and nickel with cheaper ones was proposed and Co-free Fe-Mn-(Ni) maraging steels have received increasing attention [15][16][17][18][19]. The characterisation of the precipitate and its effect on maraging behaviour have been investigated [15][20][21][22][23][24]. However, this type of Fe-Mn-(Ni) alloy suffers from severe embrittlement. Some studies suggested that the θ -NiMn precipitates resulted in the intergranular brittleness [25][26], but most studies agreed that the segregation of Mn at grain boundaries was responsible for the embrittlement [27][28][29].

Recently, Raabe and co-workers developed an alloying design strategy of combining the TRIP effect and maraging mechanism in the lean Fe-Mn alloys [30]. They reported a simultaneous increase in both strength and ductility upon aging in 12 wt.% Mn maraging TRIP steel (UTS: 1.3 GPa, TE: 21%). They attributed this effect to the combination of precipitation strengthening mechanism and TRIP effect of retained austenite [30].

In this paper, a further study is carried out on a set of Mn-based steels with minor additions of Ni, Ti and Mo. Given that Al is reported to play an active role in precipitation-strengthened steels (e.g. NiAl-strengthened steels[31][32]), ~1 wt.% Al was added on the basis of the chemical compositions given in Ref. [30]. The characterisation of precipitate using various transmission electron microscopy (TEM) techniques was performed. The microstructural evolution of reverted austenite during aging and its mechanical stability were also explored.

Particular attention was paid to the roles of precipitate and reverted austenite in the mechanical performance of the newly-developed Mn-based maraging steels.

2 Experimental

Three as-cast Mn-based steels (7-12 wt.%) were provided by Tata Steel and the chemical compositions are listed in Table 1. Figure 1 presents the equilibrium phase fractions as a function of temperature for the 10% Mn alloy as representative of other alloys. The Ae_3 temperature is 644 °C for the 10% Mn alloy. Besides the ferrite and austenite phases, the result indicates the existence of Laves phase $Fe_3Ti(Mo)$ and titanium carbide in the alloy. As this carbide is thermally stable over a large temperature range up to about 1100 °C, the homogenizing temperature is set at 1150 °C which is much higher than Ae_3 temperatures. After holding under argon gas atmosphere at 1150°C for 1 h, the three ingots were hot rolled with 85% thickness reduction between 1140 °C and 850 °C. The subsequent solution heat treatment (SHT) was conducted under argon protection at 1050 °C for 0.5 h by water quenching. Then, the solution-treated samples were aged at 460-540 °C for a range of times from 10 min to 10080 min.

Table 1 Chemical compositions (wt.%) of the studied Mn-based maraging steels

| Alloy | C | Mn | Ni | Mo | Al | Ti | Co | Fe |
|--------|-------|-------|------|------|------|------|--------|------|
| 7% Mn | 0.033 | 7.07 | 2.03 | 1.03 | 1.04 | 1.05 | <0.001 | bal. |
| 10% Mn | 0.015 | 9.97 | 2.03 | 1.19 | 1.00 | 0.84 | 0.008 | bal. |
| 12% Mn | 0.022 | 11.77 | 1.97 | 1.17 | 1.00 | 0.82 | 0.009 | bal. |

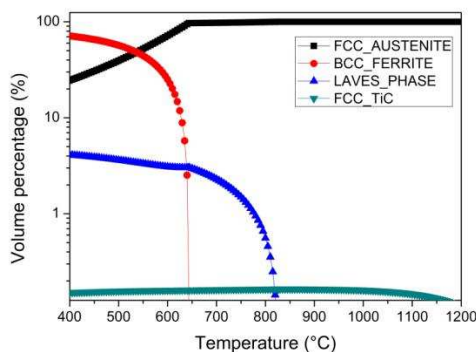


Figure 1 The equilibrium phase fractions as a function of temperature in the 10% Mn alloy, calculated by MatCalc using MC_FE_V2.0 database.

X-ray diffraction (XRD) measurements were performed on polished samples using Co K_α radiation ($\lambda = 1.78897 \text{ \AA}$) over a 2θ range of $40\text{-}130^\circ$. The qualitative and quantitative analyses were undertaken using ICDD PDF-4+ software. More than two sites of each sample were scanned for quantitative purpose.

An FEI InspectF FEG-SEM equipped with an Oxford Instruments energy-dispersive X-ray spectroscopy (EDS) was employed for microstructural observation and fractography. Samples were mechanically ground and polished with diamond suspensions to a surface finish of $1 \mu\text{m}$. The etching process was made using picric acid etchant at $60\text{-}70^\circ\text{C}$ for a few seconds. The grain size distribution of solution-treated samples was measured using a FEI Sirion FEG-SEM with an electron backscattered diffraction (EBSD) detector operated at a step size of $0.5 \mu\text{m}$. Samples for EBSD analyses were subjected to a final polishing with $0.04 \mu\text{m}$ colloidal silica suspension.

Thin foils for TEM study were prepared by a solution of 5% perchloric acid, 35% butoxyethanol and 60% methanol solution (maintained at approximately -40°C by a liquid nitrogen cooling system) running through a twin-jet electropolisher operated at $\sim 40 \text{ mA}$. In order to exclude the interference from the surrounding martensite matrix, carbon extraction replicas were made for the TEM investigation on nano-size precipitates. Low-magnification TEM observation and selected-area electron diffraction (SAED) were performed using FEI Tecnai operating at 200 kV . High resolution imaging was taken on JEOL 2010F at 200 kV . Aberration-corrected FEG JEOL R005 was utilized for scanning transmission electron microscopy (STEM) study.

Vickers hardness measurements were carried out on polished samples with a load of 294 N (30kg) and a dwell time of 15 s . Each result was averaged from at least eight measurements. Tensile testing was conducted at room temperature on a Zwick Roell Z050 tensile testing machine at a constant cross head velocity corresponding to an initial strain rate of 0.002 s^{-1} . Flat rectangular tensile samples were machined along the longitudinal direction based on ASTM standard. For nanoindentation, a cube corner tip was used for testing ultrafine austenite phase under atomic force microscope (AFM) observation. A maximum indentation load of $70 \mu\text{N}$ at a loading rate of $10 \mu\text{N/s}$ was employed.

3.1 Microstructural investigation

3.1.1 Characterisation of solution-treated structure

Figure 2 presents the XRD patterns of solution-treated 7%, 10% and 12% Mn alloys. The results reveals that only martensite was detected in the three alloys in the SHT state, which disagrees with the EBSD observation by Raabe et al. [30], who suggested that up to 15 vol.% austenite was retained after quenching in the 12 wt.% Mn alloy. Apart from the possibility that the volume fraction and size of austenite are below the detection limits of the instruments, the possible reason for this difference is that the addition of Al in this study increased the martensite start (M_s) temperature.

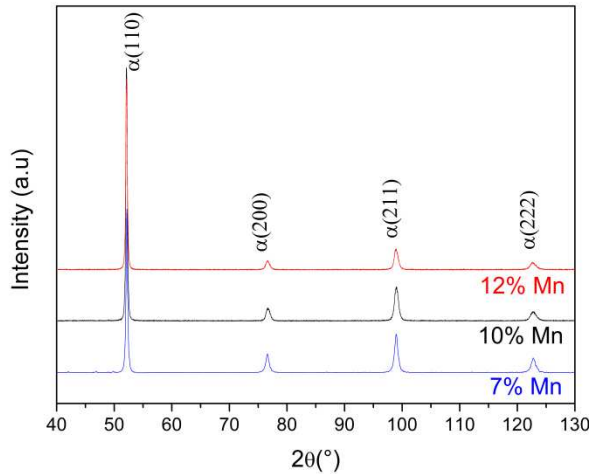


Figure 2 X-ray diffraction patterns of solution-treated 7%, 10% and 12% Mn alloys.

The grain size distribution of the 7%, 10% and 12% Mn alloys in the SHT state were characterised by EBSD and the results are displayed in Figure 3. The left column presents martensite phase (blue) with grain boundaries (black lines, $>15^\circ$). The EBSD phase maps confirm that only martensite exists in the SHT state. The right column presents the inverse pole coloured orientation maps of the same area, in which the packets of martensite laths can be clearly observed. It is evident that these martensite packets formed via water quenching possess high-angle misorientation with adjacent packets and therefore one prior austenite grain is sub-divided into several martensite packets. In other words, the effective grain size was refined owing to the dense high-angle boundaries of martensite packets. It is shown in Figure 3 that the effective grain size decreases with the increase of the Mn content of alloy,

which indicates that the Mn addition is beneficial to the grain refinement. It is generally known that the addition of Mn lowers the M_s temperatures. The reduction of M_s provides an increased driving force for phase transformation and thus a decreased driving force for the growth of martensite packets. Therefore, finer martensite packets are observed in the 12% Mn alloy compared to other two alloys.

3.1.2 Characterisation of precipitates

Representative STEM-EDS analysis was conducted along the horizontal line across precipitates in a replica sample (Figure 4). The corresponding concentration profiles of Al, Ti, Mn, Fe and Ni are plotted below the STEM micrograph. The STEM-EDS results combined with TEM-EDS analyses (presented in [33]) demonstrate that the precipitates mainly comprise Ni, Ti and Al with a small amount of Fe and Mn (Fe: ~12 at.%; Mn: ~5 at.%). In contrast to the work by Raabe and his colleagues [30][34] who speculated the precipitates were either $Ni_3(Ti,Al)$ or $NiMn/Ni_2MnAl$, the present study suggests that the chemical composition of precipitates is more likely to be non-stoichiometric Ni_2TiAl or $Ni(Ti,Al)$. This non-stoichiometry resulting from Fe and Mn segregation is proposed to increase the local disordering and dislocation climbing or cutting and thus enhance the ductility of phases [35].

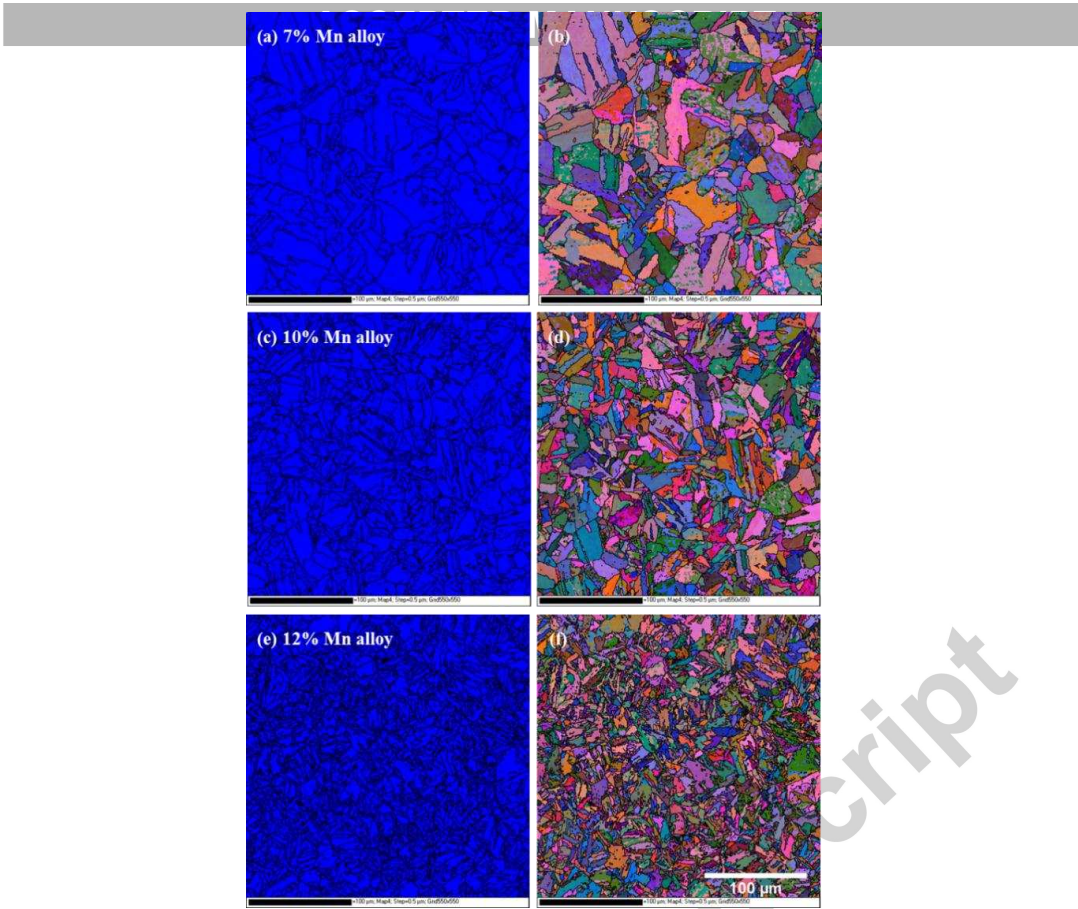


Figure 3 Microstructure of 7%, 10% and 12% Mn alloys in the SHT state by EBSD analyses. Left column: phase maps showing martensite phase (blue) with grain boundaries (black lines, $>15^\circ$). Right column: inverse pole maps of the same area, showing the orientation distribution of the martensite.

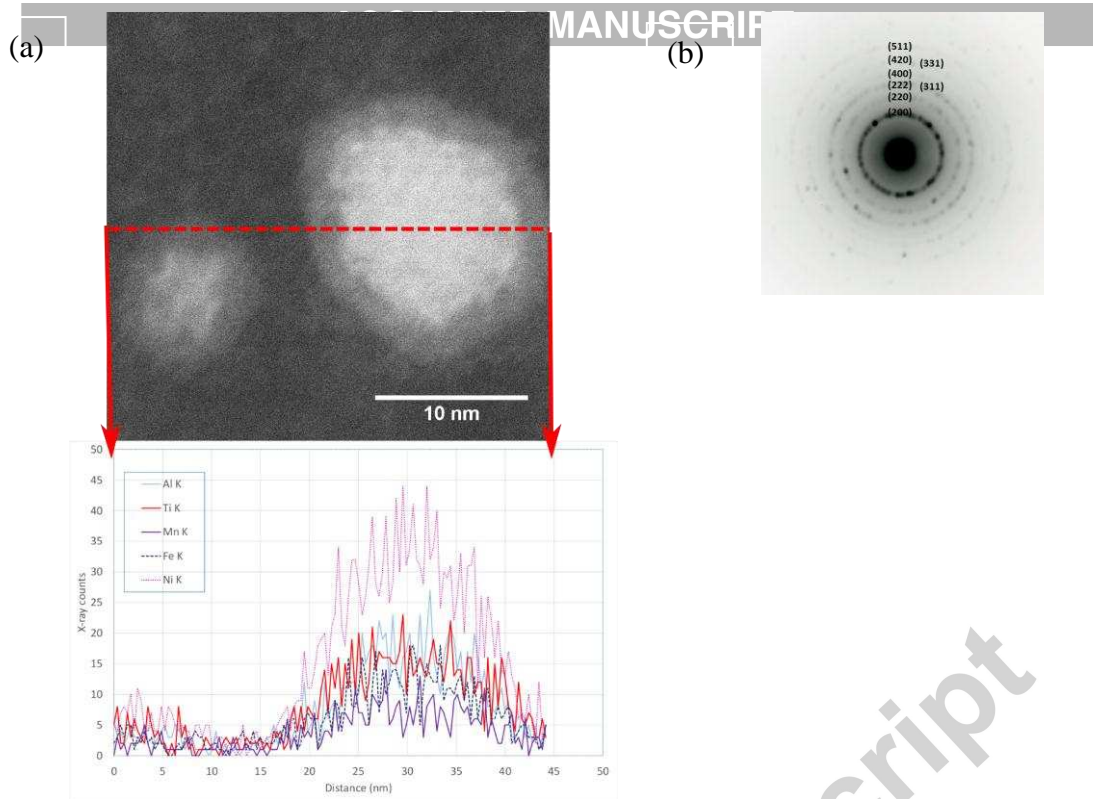


Figure 4 (a) STEM micrograph of precipitates in the 12% Mn alloy aged at 500 °C for 2880 min with STEM-EDS results of concentration profiles measured along the red line. (b) selected area diffraction pattern taken from several precipitates such as the one shown in (a), with reflections only found from the precipitates.

The crystal structure of the precipitates was studied using electron diffraction. The presence of precipitates in the dark-field image (Figure 5(a)), which was acquired by using the unique $\{11\bar{1}\}$ superlattice spots of L₂₁ structure (see inset of Figure 5(a)), demonstrates the precipitate is, or at least contain L₂₁-ordered Ni₂TiAl phase. SAED analysis also reveals that there is a cubic-on-cubic (CoC) orientation relationship between Ni₂TiAl and α' -martensite which is similar to the γ/γ' Ni-based superalloys [36]. The detail about the crystal structure is given elsewhere [33]. According to the SAED pattern, the lattice parameter of L₂₁-ordered Ni₂TiAl phase is calculated as 0.5819 nm which is in good agreement with the measurement based on high resolution micrograph of precipitate (Figure 5(b)). Half of the lattice parameter of L₂₁-ordered Ni₂TiAl is close to the lattice parameter of α -martensite matrix ($a = 0.2874$ nm) and the misfit between them is 1.24%. Owing to the small misfit of lattice parameters and the CoC orientation relationship, the L₂₁-ordered Ni₂TiAl precipitate is not only coherent but also coplanar with the α -martensite matrix. According to Ashby-Brown contrast theory [37], the dumbbell-shaped contrast observed under two-beam diffraction conditions (Figure 5(c) and (d)) confirms the precipitates remains coherent with the matrix even after aging at 500 °C for

10080 min. Figure 5(c) and (d) also reveal that this type of precipitates maintains a good resistance to coarsening after long-term aging as well as a high dispersion owing to the heavily dislocated martensite matrix providing a good nucleation condition.

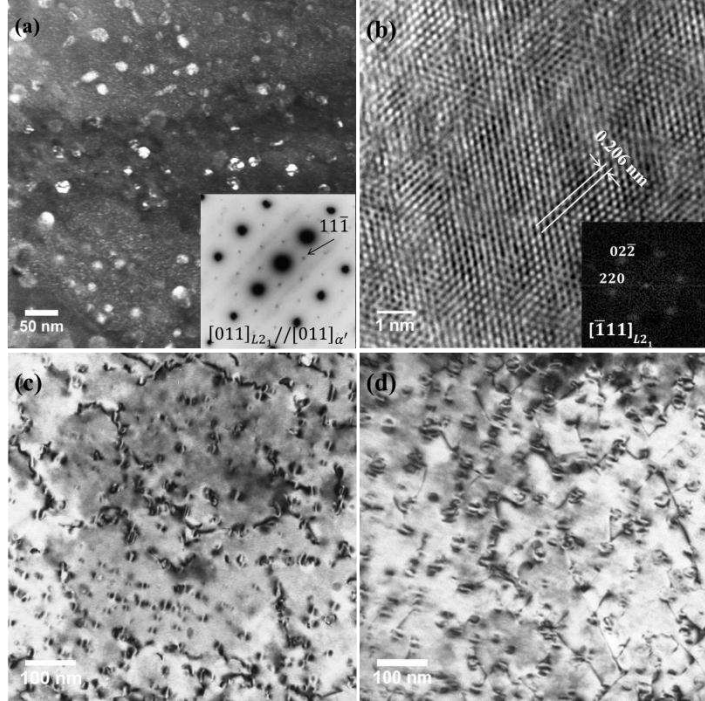


Figure 5 (a) Dark-field micrograph using the $[11\bar{1}]$ superlattice spots of precipitates (inset is the corresponding diffraction pattern); (b) High resolution micrograph of precipitates in 12% Mn alloy aged at 500 °C for 10080 min; Two-beam bright field micrographs of (c) 7% Mn alloy and (d) 10% Mn alloy aged at 500 °C /10080 min.

3.1.3 Characterisation of reverted austenite

In addition to precipitation, the aging treatment led to the formation of reverted austenite. However, X-ray diffraction results reveal that austenite was only observed in the overaged 10% and 12% Mn alloys, and no peaks related to precipitates were detected (Figure 6(a)). Additional peaks were observed in the samples aged at 500 °C for a long period. These peaks were shown to be ϵ -martensite which was transformed from austenite upon cooling after heat treatment by a diffusionless mechanism [38][39].

The volume fractions of reverted austenite in the 10% and 12% Mn alloys in different conditions are shown in Figure 6(b). The austenite fraction of the 12% Mn alloy is obviously higher than that of the 10% Mn alloy for the same aging condition. In addition, it is apparent that the austenite reversion in the 12% Mn alloy kinetically exceeded that in the 10% Mn alloy,

which is associated with more grain boundaries as nucleation sites for austenite reversion in the 12% Mn alloy. Aging at 500 °C led to a nearly linear increase in the volume fraction of reverted austenite until a maximum was reached (10% Mn alloy: ~10.7 vol.% at 10080 min; 12% Mn alloy: ~24.8 vol.% at 4320 min). After the maximum, the phase fraction tended to stay approximately constant with further aging. It is worth noting that the equilibrium volume fraction of austenite is significantly lower than that predicted by MatCalc (Figure 1), which is suggested to partially result from $\gamma \rightarrow \epsilon$ martensitic transformation. This $\gamma \rightarrow \epsilon$ martensitic transformation was also responsible for the slight decrease in the volume fraction of reverted austenite with aging time in Figure 6(b).

As the experimental evidence revealed that no austenite was retained after water quenching from the SHT, the entire austenite in the aged samples is regarded as a product of austenite reversion from martensite. The microstructural evolution of reverted austenite during aging is presented in Figure 7. Initially, thin austenite layers were generated mainly along prior austenite grain boundaries and martensite packet boundaries (Figure 7(a)). During the subsequent aging, austenite layers were formed within the martensite laths and these austenite layers then gradually grew to lath-like austenite grains (Figure 7(b) and (c)). The analysis of the size of the reverted austenite reveals that lath-like reverted austenite was resistant to growth in the lateral direction, with the thickness remaining below ~200 nm when aged at 500 °C.

EDS in the TEM was used to examine the chemical composition of reverted austenite in the three alloys under different aging conditions. In the initial stages of austenite reversion, along with the Mn and Fe enrichment, a considerable amount of Ti and Mo was detected at grain boundaries, as shown in Figure 8(a). This finding is surprising as Ti is generally considered to raise A_e^3 temperature and therefore the segregation of Ti at grain boundaries should suppress austenite formation. On the other hand, a significant increase in the Mn concentration accompanied with a decrease in Ti and Mo concentrations was observed as austenite grains grew (Figure 8(b)). TEM-EDS reveals that lath-like austenite grains have an average of Mn concentration of ~24 at.%.

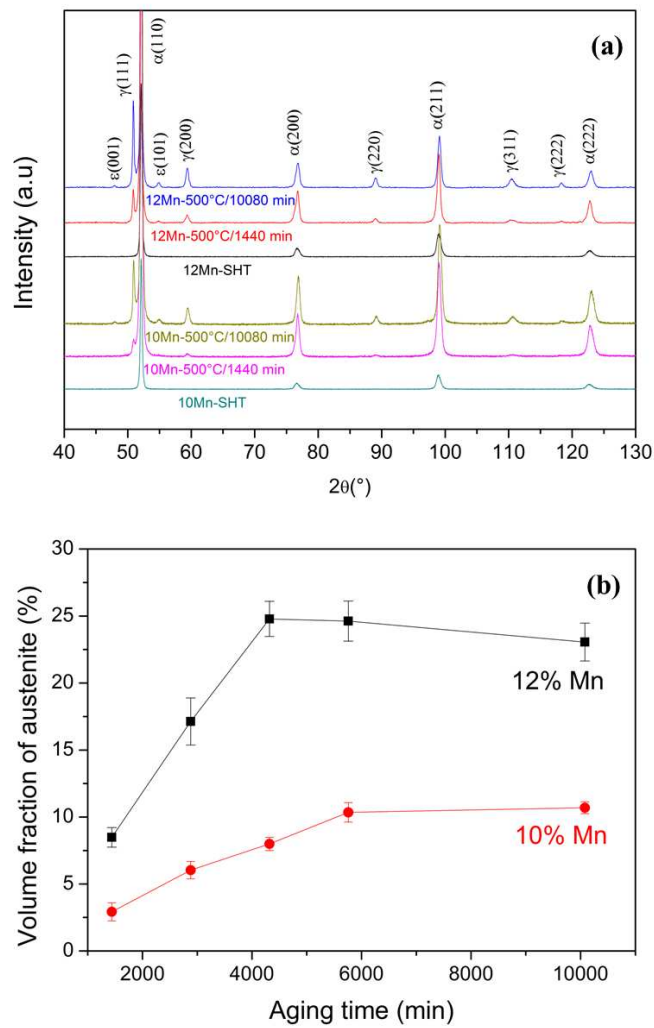


Figure 6 (a) X-ray diffraction patterns of 10% and 12% Mn alloys in the SHT state and aged at 500 °C for different durations; (b) evolution of volume fractions (vol.%) of reverted austenite formed as a function of aging time at the temperature of 500 °C.

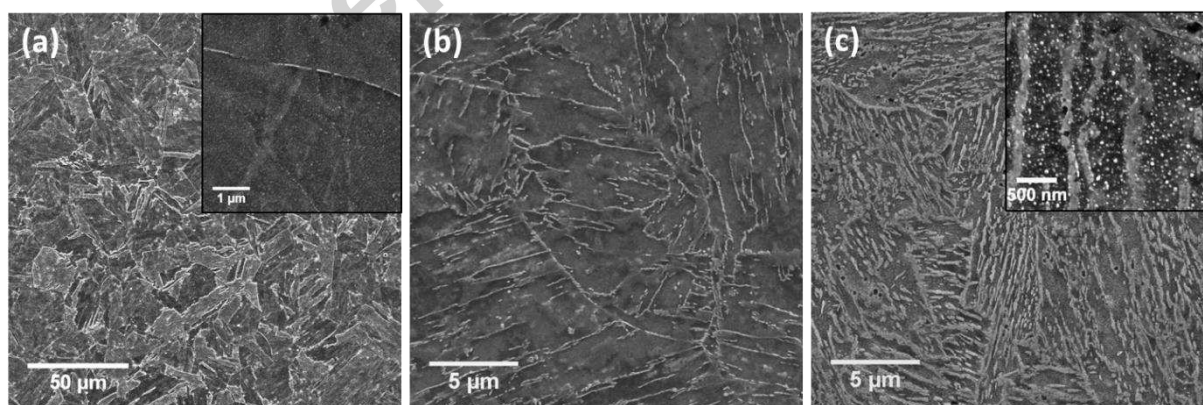


Figure 7 SEM micrographs of reverted austenite in the 12% Mn alloy in (a) 500 °C / 10 min state, (b) 500 °C / 1440 min state, (c) 500 °C / 10080 min state.

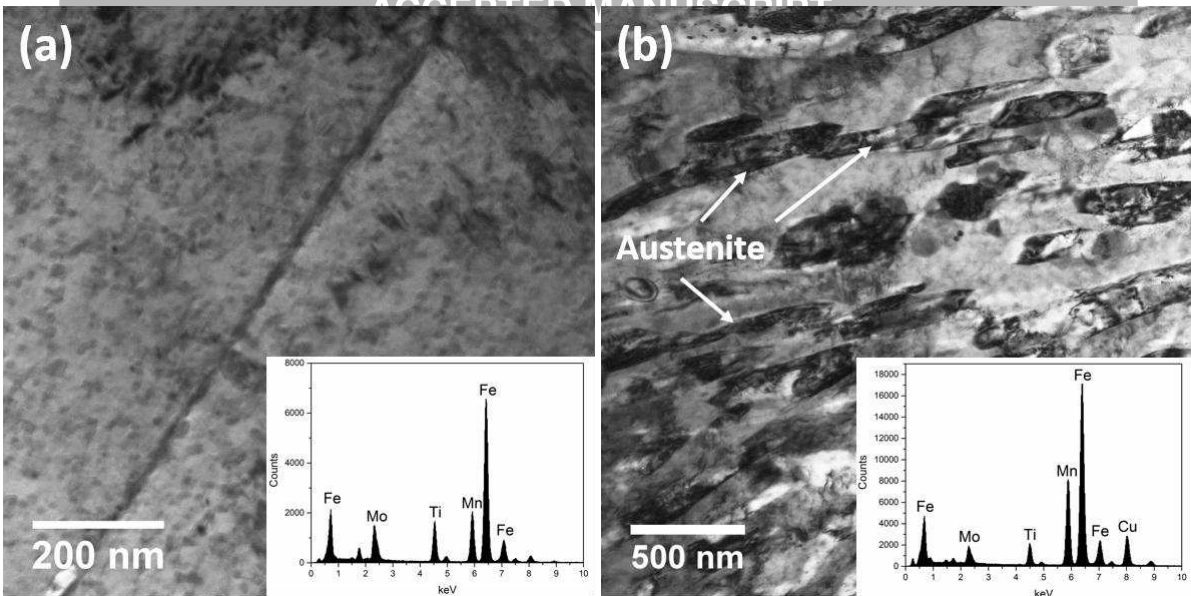


Figure 8 TEM micrographs and corresponding TEM-EDS spectra (inset) of reverted austenite in (a) 10% Mn alloy, 500 °C / 1440 min and (b) 12% Mn alloy, 540 °C / 2880 min.

3.2 Mechanical properties

3.2.1 Hardness evolution

Figure 9 displays the hardness as a function of time for Mn-based maraging steels aged at different temperatures. It is apparent that the three alloys exhibit a typical hardness evolution of precipitation-strengthened alloys. Aging at 460 °C led to the peak hardness in the 10% Mn and 12% Mn alloys, but the 7% Mn alloy experienced a long incubation and aging time that did not achieve a peak hardness in the time investigated (Figure 9(a)). The 12% Mn alloy was the first that reached the maximum hardness (453 HV, 480 min), followed by the 10% Mn alloy (457 HV, 1440 min) and then the 7% Mn alloy (454 HV, 5760 min). A more rapid increase of hardness was observed in the early aging stage of the 10% and 12% Mn alloys aged at 500 °C, over 90% of the total increase in hardness was achieved within the first 30 minutes (Figure 9(b)). Despite the difference in the hardening kinetics, the maximum hardness of the three alloys are very close (7% Mn alloy: 418 HV at 240 min; 10% Mn alloy: 421 HV at 240 min; 12% Mn alloy: 432 HV at 120 min). It is worth highlighting that in the overaged region, what appears to be secondary hardening was observed in both 10% Mn and 12% Mn alloy, which suggests that an additional phase may have contributed to the hardening.

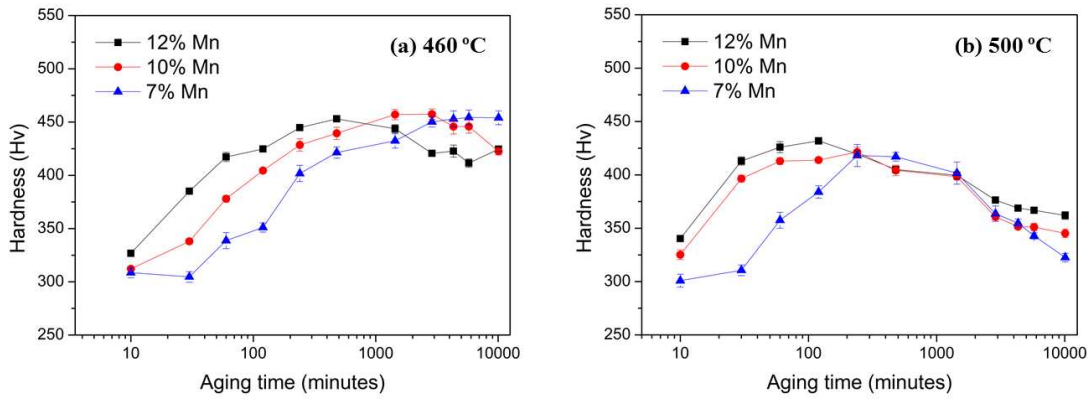


Figure 9 The evolution of Vickers hardness in the 7% Mn, 10% Mn and 12% Mn alloy aged at (a) 460 °C and (b) 500 °C, respectively.

3.2.2 Tensile testing

Although impressive tensile properties have been reported in other Mn-based steels [1][4][8][14], the mechanical properties of 10% Mn and 12% Mn alloys listed in Table 2 are still remarkable compared to those reported with the same level of carbon content (~0.03 wt.%). It is found that the yield strength (YS), UTS and tensile elongation (TE) in the SHT state increase with the Mn content of alloy, but the differences among the three alloys are small. After aging, the three alloys suffered from poor ductility for short aging times. Prolonged aging treatment significantly improved the embrittlement but was detrimental to the strength. For the 7% Mn alloy, most of the aged samples failed before approaching the yield point. Only the sample in the 500 °C / 10080 state exhibited a limited TE of 6.6% (Table 2). For the 10% Mn alloy, an evident elongation of 12.1% with a UTS of 1113 MPa was achieved after aging at 500 °C for 2880 min. Further aging for 5760 min led to a increase in TE to 17.0% but a slight decrease in UTS of 1062 MPa. For the 12% Mn alloy, the improvement of the ductility was even faster. A substantial UTS of 1306 MPa with a ductility (TE: 5.5%) was achieved after a short aging time (240 min). Extended aging to 2880 min led to a significant increase in ductility (17.8%) but a decrease in strength (1142 MPa). At the end of aging treatment, further aging up to 5760 min did not result in any obvious variation in the mechanical properties (Table 2).

Table 2 Summary of YS, UTS and TE for three alloys in different heat-treatment conditions.

| | YS (MPa) | UTS (MPa) | TE (%) |
|---------------------------|----------|-----------|--------|
| 7% Mn, SHT | 748 | 852 | 6.9 |
| 7% Mn, 500° C / 10080 min | 933 | 1005 | 6.6 |
| 10% Mn, SHT | 795 | 882 | 7.1 |
| 10% Mn, 500° C / 2880 min | 1002 | 1113 | 12.1 |
| 10% Mn, 500° C / 5760 min | 876 | 1062 | 17.0 |
| 12% Mn, SHT | 834 | 931 | 7.5 |
| 12% Mn, 500° C / 240 min | 1250 | 1306 | 5.5 |
| 12% Mn, 500° C / 1440 min | 994 | 1137 | 7.6 |
| 12% Mn, 500° C / 2880 min | 948 | 1142 | 17.8 |
| 12% Mn, 500° C / 5760 min | 882 | 1120 | 18.4 |

Figure 10 displays the fracture surfaces of the 12% Mn alloy in different conditions. The 12% Mn alloy in the SHT state reveals a complete transgranular ductile fracture with bimodal dimples (Figure 10(b)). Although intergranular brittleness occurred in the beginning of aging at 500 °C (Figure 10(c)), further aging significantly improved the fracture performance. In the 500 °C / 240 min state, the fracture mode transformed to quasi cleavage fracture mode (Figure 10(d)). The quasi cleavage is similar to the cleavage fracture but with an increased ductile proportion (see inset). After aging for 1440 min, a microvoid coalescence fracture mode was present with a small amount of river pattern (Figure 10(e)). Obvious necking and large reduction in area are observed in the 500 °C / 5760 min state and the fractograph was completely dimple fracture mode (Figure 10(f)). These dimples in aged samples are much smaller and shallower compared to those in the SHT state (Figure 10 (b)).

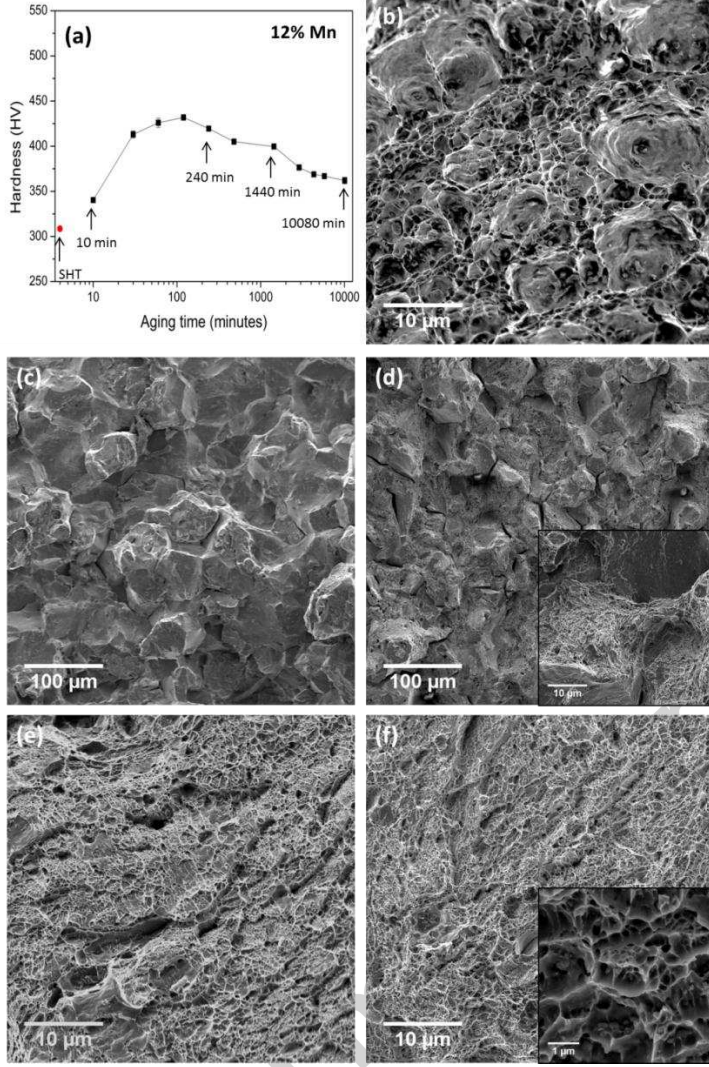


Figure 10 (a) The hardness evolution of 12% Mn alloy aged at 500 °C and the fracture surface (b) in the SHT state and aged at 500 °C for (c) 10 min; (d) 240 min; (e) 1440 min and (f) 5760 min.

3.2.3 Nanoindentation

Nanoindentation was undertaken to study the mechanical characteristic of each phase and its contribution to the strength. The typical load-displacement ($P-h$) curves of austenite and martensite are illustrated in Figure 11. Different phases are characterised by different load-displacement relationships, i.e., the maximum penetration displacement is 10-15 nm for austenite phase and ~25 nm for martensite phase (Figure 11(a)). The reverted austenite was unexpectedly harder than the martensite. It is recognized that austenite, as a fcc crystal, has a low yield strength, especially compared to the martensite with highly dispersed nanoprecipitates. Despite the low yield strength, the austenite generally exhibits extensive work hardening. The hardness of each phase in different samples was measured and the results

are displayed in Figure 11(b) and (c). The austenite hardness of the 12% Mn alloy aged at 500 °C for 10080 min is higher than that of the 10% Mn alloy for the same aging condition whereas the martensite hardness of the 12% Mn alloy is slightly lower than that of the 10% Mn alloy (Figure 11(b)). In terms of the effect of aging temperature, it is clearly shown in Figure 11(c) that the hardness of both the austenite and martensite decrease as the aging temperature increases.

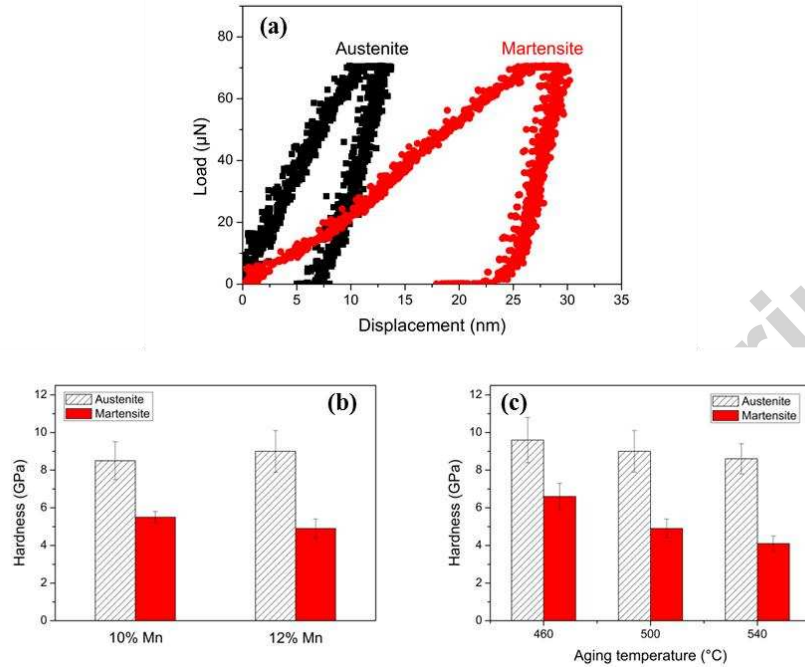


Figure 11 (a) Load-displacement curves of martensite and austenite in 12% Mn alloy (500 °C / 10080 min); (b) The average hardness of austenite and martensite in 10% Mn and 12% Mn alloys aged at 500 °C for 10080 min and (c) the hardness of austenite and martensite in 12% Mn alloy as a function of aging temperature.

4 Discussion

The strengthening mechanism of metal is generally expressed as:

$$\sigma_y = \sigma_B + \sigma_{SS} + \sigma_{GR} + \sigma_{PH} + \sigma_{SH} \quad (1)$$

where σ_y is the total yield strength, σ_B is the yield strength of base steel, σ_{SS} is the solid-solution strengthening, σ_{GR} is the grain refinement strengthening, σ_{PH} is the precipitation strengthening and σ_{SH} is the strain hardening. However, the strengthening mechanism in steels

is more complex. The multiphase in steels may have different contributions to strengthening. Besides, the phase transformation may also be involved.

4.1 Solid-solution and grain refinement strengthening in the SHT state

In the SHT state, the strengthening mechanism is mainly constituted by solid-solution and grain refinement strengthening. Since a large amount of solute (e.g. Mn, Ni, Ti, Al and Mo) was added, the solid solution strengthening of Mn-based maraging steels in this study is substantially increased when compared to that of the base steel. The strengthening by substitutional solute atoms generally increases with the difference in atomic size between the solute and Fe. On the other hand, the difference in the elastic behaviour of solute and solvent atoms is also important in determining the overall solid solution strengthening [40]. Although Mn is an effective strengthener in Fe alloy, other elements, such as Mo and Al, have more significant effect. Hence, the differences of solid-solution strengthening among the three alloys are supposed to be small. In terms of grain refinement strengthening, although the Mn addition significantly refines martensite packets (Figure 3), it is thought that the martensite packets boundaries are too weak to resist dislocations and thus the grain refinement strengthening is negligible compared to solid-solution strengthening. Therefore, the YS in the SHT state (Table 2) indeed increases as the Mn content of alloy increases, but the differences among the three alloys are small.

4.2 Precipitation strengthening mechanism in peak-aged condition

The precipitation strengthening is based on the interaction between dislocations and precipitates whereby the dislocation loop or bow around the precipitates via Orowan mechanism [41]:

$$\sigma_y = \sigma_0 + \frac{T}{b\Lambda} \quad (2)$$

where σ_0 is the sum of other strengthening mechanisms, T is the line tension, b is the Burgers vector and Λ is the interparticle spacing. Ansell and his colleagues [42][43] proposed a modified form of the Orowan equation in which σ_y can be expressed as:

$$\sigma_y = \sigma_0 + \frac{2Gb\emptyset\ln(\Lambda-d/2b)}{4\pi(\Lambda-d)} \quad (3)$$

where G is the shear modulus of matrix, \emptyset is related to the Poisson's ratio of matrix by $\emptyset = \left[1 + \frac{1}{1-v}\right]/2$ and d is the mean size of precipitates. In this study, the peak hardness condition was considered to be mainly attributed to precipitation. However, in order to avoid the effect of intergranular brittleness, the yield strength of a slightly overaged sample (12%

Mn alloy, 500 °C / 240 min state) is studied to estimate the precipitation strengthening mechanism. This sample has a small amount of reverted austenite (< 3 vol.%) , so the effect of reverted austenite on strengthening would have been negligible. The value of σ_0 is assumed to be equal to that of σ_y in the SHT state. The average precipitate size was measured as 7.4 nm and the interpartical spacing is ~40 nm. Taking $G = 71$ GPa [19], $|b| = 0.249$ nm [44], $v = 0.3$ [45] and $\sigma_0 = 820$ MPa, the calculated σ_y is 1258 MPa which is in good agreement with the experimental value (~1250 MPa). As a result of precipitation strengthening, the peak-aged sample exhibits a better work hardening compared to the sample in the SHT state (Figure 12). However, the ductility, like other conventional maraging steels, is still unsatisfactory.

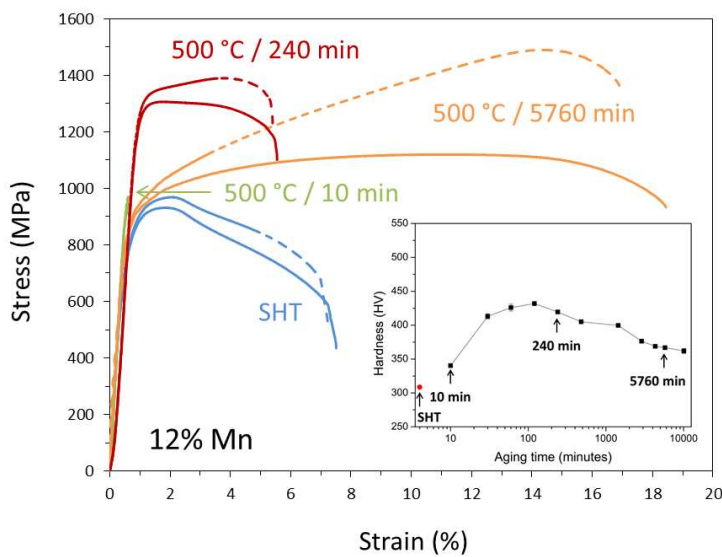


Figure 12 The engineering stress-strain curves (solid lines) and true stress-strain curves (dash lines) of 12% Mn alloy in different heat treatment conditions.

4.3 Austenite engineering in overaged conditions

Based on the Orowan mechanism, it is not surprising to see a decrease in yield strength due to the coarsening of precipitates during the overaged period. However, the experimental σ_y in the 500 °C / 5760 min state (882 MPa) was much lower than the value (1090 MPa) given by Equation (3). Generally, the loss of strength was considered to be related to the formation of reverted austenite in the overaged state. However, in these alloys the hardness of reverted austenite was found to be even higher than that of α' -martensite (Figure 11). Therefore, this discrepancy is considered to be mainly attributed to two factors: (i) the precipitation and austenite reversion for the longer aging times consumed a large amount of solute, which

weakened the solid-solution strengthening of α' -martensite; (ii) the annihilation of dislocation slip as a result of the recovery of α' -martensite during long-term aging would have reduced its strength.

Despite the relatively low yield strength, the 12% Mn alloy in the 500 °C / 5760 min state exhibit steady work hardening after the yield point which greatly enhanced the strength (Figure 12). This work hardening apparently compensated the loss of yield strength after long-term aging, and more importantly, it was accompanied by an increase in ductility.

4.3.1 The stability of reverted austenite

The stability of austenite is generally governed by the chemical composition [5][13][46], grain size [13][47][48][49][50], morphology [51] and adjacent microstructure [46][52][53], among which the chemical composition and grain size are considered as the two primary contributors [13][54]. The morphology of austenite and its adjacent microstructure is important for the stability in the case that film-like retained austenite are shielded by bainitic ferrite or martensite [46][51].

In terms of the chemical composition, the Mn concentration is considered to be the most crucial factor to determine the stability of austenite in the present alloys. The TEM-EDS measurements reveal that lath-like reverted austenite formed at 500 °C for a long aging time has a high Mn concentration up to 24 at.%. Such a Mn concentration in the reverted austenite in Mn-based maraging steels is significantly higher than that of retained austenite (8-12 at.% Mn) reported in Mn TRIP steels [1][13][55] and is suggested to be responsible for the high stability of reverted austenite. Yen et al. [5] reported that the compositional difference in austenite could lead to a significant variation in the efficiency of the TRIP effect. According to their study, an additional stress of 587 MPa was required to assist the deformation-induced α' -martensitic transformation with 2.6 wt.% higher Mn concentration.

The effect of the reverted austenite grain size is a matter of debate. It is generally accepted that finer grain size of austenite suppresses the martensitic transformation and contributes to the stability [13][47][48]. In contrast, Wang [49] suggested that the outer layer of reverted austenite with lower concentration of austenite stabilizing elements has a higher potential to transform into martensite. Hence larger austenite grains with a lower fraction of outer layer is more stable. In addition, Wang et al. [50] proposed a ‘smaller is less stable’ effect of austenite in a 9Mn TRIP-maraging steel since they observed that mechanical twinning was less likely to occur in smaller austenite grains. In the present work, the reverted austenite did not grow significantly in the lateral direction, whereas the Mn concentration did change appreciably

during aging. Therefore, the present work has not found any evidence supporting the above viewpoints. Further work is clearly needed to focus on the effect of the reverted austenite size and morphology on its stability.

XRD and microstructural investigation on deformed tensile samples (Figure 13) indicates that plastic deformation did not lead to a significant decrease in the amount of austenite. A more evident decrease in the volume fraction of austenite after tensile testing is found in the 10% Mn alloy, which may be associated with a lower stability of austenite due to lower Mn concentration in austenite (detailed correlation between the stability of austenite and Mn content is given in [56]). In contrast to the TRIP effect extensively reported in Mn-based TRIP or Q&P steels [1][2][5][8], all the evidence in this study indicates that the reverted austenite in Mn-based maraging steels exhibited high stability against deformation-induced martensitic transformation, and so the TRIP effect was not a factor in the tensile deformation behaviour.

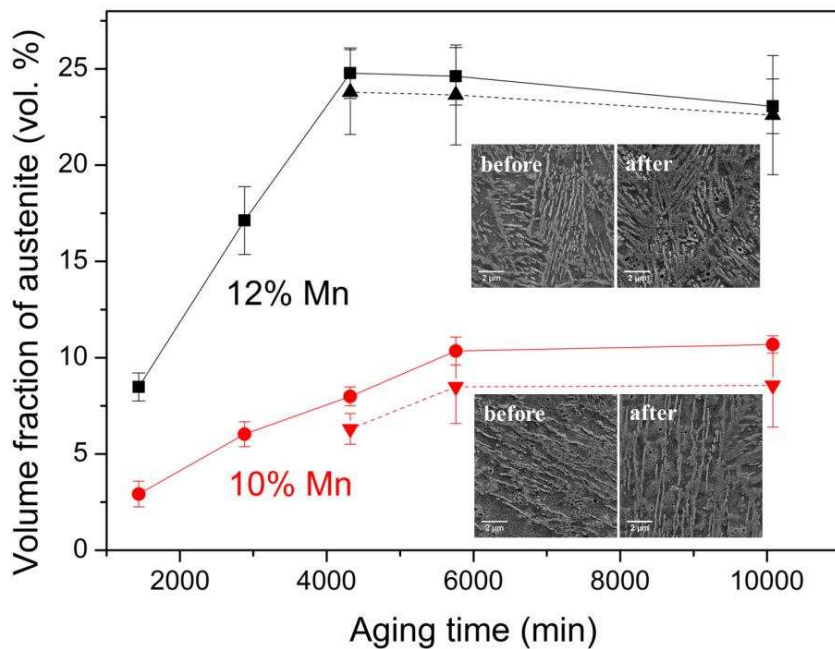


Figure 13 Volume fraction of reverted austenite as a function of aging time at the temperature of 500 °C (solid lines: before tensile testing; dash lines: after tensile testing).

4.3.2 The effect of reverted austenite on work hardening behaviour

The XRD and hardness analyses indicate that the secondary hardening in the overaged period was associated with austenite reversion (Figure 14), e.g. a certain amount of austenite (can be detected by XRD, >3 vol.%) in the 10% Mn alloy was generated after aging at 500 °C for

1440 min, which coincides with the initiation of secondary hardening. Although austenite layers had formed earlier before the 500 °C / 1440 min state, it is not believed that the ultrathin austenite layers contributed greatly to the strength. In addition, nanoindentation testing also reveals that lath-like reverted austenite is even harder than tempered martensite matrix.

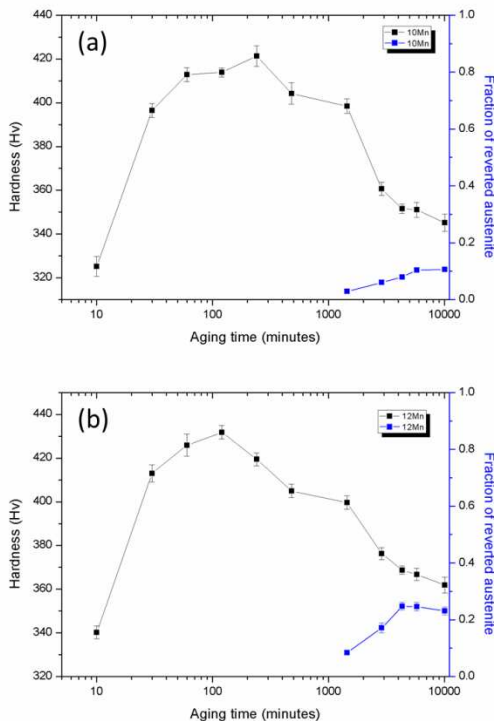


Figure 14 Hardness evolution vs. volume fraction of austenite as a function of time in (a) 10% Mn and (b) 12% Mn alloys when aged at 500 °C.

The improvement in ductility is attributed to the inherently greater ductility of austenite phase rather than TRIP effect. The fractographs (Figure 10) and high resolution TEM-EDS (Figure 8) studies suggest that intergranular brittleness in the initial stage of aging resulted from the segregation of Mn at grain boundaries which increased the ductile-brittle transition temperature (DBTT). Although the subsequent formation of austenite layers gradually removed the embrittlement, the ductility was still unsatisfactory. Only after further aging was the ductility significantly improved by the formation of ductile lath-like austenite. Increasing aging temperature or the Mn content of the alloy that promoted austenite reversion was demonstrated to accelerate the improvement of ductility (Table 2). However, once tensile ductility was achieved, a further increase in the amount of reverted austenite did not lead to a corresponding improvement in ductility, e.g. the higher amount of austenite in 12% Mn alloys

than 10% Mn alloy in the 500°C / 5760 min state (10.4 vol.% vs. 24.6 vol.%) did not lead to an evident advance in ductility (Table 2). This evidence confirms that the TRIP effect of reverted austenite did not occur to any significant amount in Mn-based maraging steels, although the observed ductility was approximately proportional to the volume fraction of austenite, consistent with observations in TRIP steels [57].

5 Conclusions

The addition of Mn has been demonstrated to greatly refine martensite packets via reducing the M_s temperatures. However, as the grain boundaries of martensite packets are too weak, the grain-refinement strengthening via Mn addition is negligible. Therefore, solid-solution strengthening is the dominant mechanism of Mn-based maraging steels in the SHT state. The addition of a large number of solute atoms (e.g. Mn, Ni, Ti, Al and Mo) strongly strengthened the materials. Although Mn is an effective strengthener, other elements, such as Mo and Al, have more significant effect. Therefore, the variation of the Mn content did not lead to evident difference in the strength among the three alloys.

The precipitates formed in Mn-based maraging steels were characterised as L2₁-ordered Ni₂TiAl phase. This type of precipitate formed a coherent-coplanar orientation relationship and maintained a good resistance to coarsening and high dispersion within martensite matrix even after long aging treatment. Evidence reveals that Fe and Mn also participated in the formation of precipitates. Higher Mn content of alloy led to a faster precipitation reaction and thus a faster hardening kinetics. Tensile performance suggests that the improved yield strength of peak-aged samples was mainly attributed to the formation of Ni₂TiAl precipitates and the precipitation strengthening was governed by Orowan mechanism.

The 10% and 12% Mn alloys in the overaged condition exhibited steady work hardening during deformation. This increase in strength after the yield point apparently compensated the loss of yield strength resulting from the coarsening of precipitates and recovery of α' -martensite matrix after long-term aging. No TRIP effect was observed from the reverted austenite, since the thin reverted austenite that contained a high Mn concentration exhibited high stability against transformation. In addition, the improvement in ductility in the overaged stage was also attributed to the inherently greater ductility of austenite phase rather than the TRIP effect.

The authors are grateful to Tata Steel for providing the materials studied in this work. Special thanks go to Dr Lin Sun for performing thermodynamic calculation by MatCalc. China Scholarship Council (CSC) and Department for Business, Innovation & Skills (BIS) are greatly acknowledged for the award of a scholarship to Feng Qian for studying at University of Sheffield.

References

- [1] H. Luo, J. Shi, C. Wang, W. Cao, X. Sun, and H. Dong, "Experimental and numerical analysis on formation of stable austenite during the intercritical annealing of 5Mn steel," *Acta Materialia*, vol. 59, no. 10, pp. 4002–4014, Jun. 2011.
- [2] D.-W. Suh, S.-J. Park, T.-H. Lee, C.-S. Oh, and S.-J. Kim, "Influence of Al on the Microstructural Evolution and Mechanical Behavior of Low-Carbon, Manganese Transformation-Induced-Plasticity Steel," *Metallurgical and Materials Transactions A*, vol. 41, no. 2, pp. 397–408, Dec. 2009.
- [3] H. Ghassemi-Armaki, R. Maaß, S. P. Bhat, S. Sriram, J. R. Greer, and K. S. Kumar, "Deformation response of ferrite and martensite in a dual-phase steel," *Acta Materialia*, 2013.
- [4] P. J. Gibbs, E. De Moor, M. J. Merwin, B. Clausen, J. G. Speer, and D. K. Matlock, "Austenite Stability Effects on Tensile Behavior of Manganese-Enriched-Austenite Transformation-Induced Plasticity Steel," *Metallurgical and Materials Transactions A*, vol. 42, no. 12, pp. 3691–3702, Apr. 2011.
- [5] H.-W. Yen, S. W. Ooi, M. Eizadjou, A. Breen, C.-Y. Huang, H. K. D. H. Bhadeshia, and S. P. Ringer, "Role of stress-assisted martensite in the design of strong ultrafine-grained duplex steels," *Acta Materialia*, vol. 82, pp. 100–114, Jan. 2015.
- [6] R. L. Miller, "Ultrafine-grained microstructures and mechanical properties of alloy steels," *Metallurgical Transactions*, vol. 3, no. 4, pp. 905–912, Apr. 1972.
- [7] M. Niikura and J. W. Morris, "Thermal processing of ferritic 5Mn steel for toughness at cryogenic temperatures," *Metallurgical Transactions A*, vol. 11, no. 9, pp. 1531–1540, Sep. 1980.
- [8] J. Han, S.-J. Lee, J.-G. Jung, and Y.-K. Lee, "The effects of the initial martensite microstructure on the microstructure and tensile properties of intercritically annealed Fe–9Mn–0.05C steel," *Acta Materialia*, vol. 78, pp. 369–377, Oct. 2014.
- [9] T. Furukawa, "Dependence of strength–ductility characteristics on thermal history in lowcarbon, 5 wt-%Mn steels," *Materials Science and Technology*, vol. 5, no. 5, p. 465, Jul. 1989.
- [10] T. Furukawa, H. Huang, and O. Matsumura, "Effects of carbon content on mechanical properties of 5%Mn steels exhibiting transformation induced plasticity," *Materials Science and Technology*, vol. 10, no. 11, p. 964, Jul. 1994.
- [11] D. W. Suh, J. H. Ryu, M. S. Joo, H. S. Yang, K. Lee, and H. K. D. H. Bhadeshia,

- [12] B. C. De Cooman, P. Gibbs, S. Lee, and D. K. Matlock, “Transmission Electron Microscopy Analysis of Yielding in Ultrafine-Grained Medium Mn Transformation-Induced Plasticity Steel,” Metallurgical and Materials Transactions A, vol. 44, no. 6, pp. 2563–2572, Feb. 2013.
- [13] S. Lee, S.-J. Lee, and B. C. De Cooman, “Austenite stability of ultrafine-grained transformation-induced plasticity steel with Mn partitioning,” Scripta Materialia, vol. 65, no. 3, pp. 225–228, Aug. 2011.
- [14] J. Shi, X. Sun, M. Wang, W. Hui, H. Dong, and W. Cao, “Enhanced work-hardening behavior and mechanical properties in ultrafine-grained steels with large-fractioned metastable austenite,” Scripta Materialia, vol. 63, no. 8, pp. 815–818, Oct. 2010.
- [15] J. Singh and C. M. Wayman, “Age-hardening characteristics of a martensitic Fe-Ni-Mn alloy,” Materials Science and Engineering, vol. 94, pp. 233–242, Oct. 1987.
- [16] N.-H. Heo, “Theory of nonequilibrium segregation in an Fe-Mn-Ni ternary alloy and a ductile-brittle-ductile transition,” Acta Materialia, vol. 44, no. 7, pp. 3015–3023, Jul. 1996.
- [17] S. Hossein Nedjad, M. Nili Ahmadabadi, and T. Furuhara, “Transmission Electron Microscopy Study on the Grain Boundary Precipitation of an Fe-Ni-Mn Maraging Steel,” Metallurgical and Materials Transactions A, vol. 39, no. 1, pp. 19–27, 2008.
- [18] L.-T. Shiang and C. M. Wayman, “Maraging behavior of an Fe-19.5Ni-5Mn alloy. III: Mechanical properties,” Metallography, vol. 22, no. 1, pp. 15–36, Jan. 1989.
- [19] S. J. Kim and C. M. Wayman, “Strengthening behaviour and embrittlement phenomena in Fe-Ni-Mn-(Ti) maraging alloys,” Materials Science and Engineering: A, vol. 207, no. 1, pp. 22–29, 1996.
- [20] L. T. Shiang and C. M. Wayman, “Maraging behavior in an Fe-19.5Ni-5Mn alloy I: Precipitation characteristics,” Metallography, vol. 21, no. 4, pp. 399–423, Nov. 1988.
- [21] S.-H. Mun, M. Watanabe, D. B. Williams, X. Li, K. Hwan Oh, and H.-C. Lee, “Precipitation of austenite particles at grain boundaries during aging of Fe-Mn-Ni steel,” Metallurgical and Materials Transactions A, vol. 33, no. 4, pp. 1057–1067, Apr. 2002.
- [22] Y.-U. Heo, M. Takeguchi, K. Furuya, and H.-C. Lee, “Discontinuous coarsening behavior of Ni₂MnAl intermetallic compound during isothermal aging treatment of Fe–Mn–Ni–Al alloys,” Journal of Electron Microscopy, vol. 59, no. S1, pp. S135–S140, 2010.
- [23] S.-J. Kim and C. M. Wayman, “Electron microscopy study of precipitates in Fe-Ni-Mn maraging alloys,” Materials Science and Engineering: A, vol. 136, pp. 121–129, Apr. 1991.
- [24] E. V Pereloma, R. A. Stohr, M. K. Miller, and S. P. Ringer, “Observation of precipitation evolution in Fe-Ni-Mn-Ti-Al maraging steel by atom probe tomography,” Metallurgical and Materials Transactions A: Physical Metallurgy and Materials Science, vol. 40, no. 13, pp. 3069–3075, 2009.
- [25] H.-C. Lee, S.-H. Mun, and D. McKenzie, “Electron microscopy study on the grain-boundary precipitation during aging of Fe-10Ni-5Mn steel,” Metallurgical and Materials Transactions A, vol. 34, no. 11, pp. 2421–2428, Nov. 2003.
- [26] S. Hossein Nedjad, M. Nili Ahmadabadi, and T. Furuhara, “Correlation between the intergranular brittleness and precipitation reactions during isothermal aging of an Fe–

- [27] D. R. Squires and E. A. Wilson, “Aging and brittleness in an Fe-Ni-Mn alloy,” Metallurgical Transactions, vol. 3, no. 2, pp. 579–585, Feb. 1972.
- [28] N.-H. Heo and H.-C. Lee, “The embrittlement and de-embrittlement of grain boundaries in an Fe-Mn-Ni alloy due to grain boundary segregation of Mn,” Metallurgical and Materials Transactions A, vol. 27, no. 4, pp. 1015–1020, Apr. 1996.
- [29] N. H. Heo, J. W. Nam, Y. U. Heo, and S. J. Kim, “Grain boundary embrittlement by Mn and eutectoid reaction in binary Fe–12Mn steel,” Acta Materialia, vol. 61, no. 11, pp. 4022–4034, 2013.
- [30] D. Raabe, D. Ponge, O. Dmitrieva, and B. Sander, “Designing Ultrahigh Strength Steels with Good Ductility by Combining Transformation Induced Plasticity and Martensite Aging,” Advanced Engineering Materials, vol. 11, no. 7, pp. 547–555, 2009.
- [31] Z. Sun, C. H. Liebscher, S. Huang, Z. Teng, G. Song, G. Wang, M. Asta, M. Rawlings, M. E. Fine, and P. K. Liaw, “New design aspects of creep-resistant NiAl-strengthened ferritic alloys,” Scripta Materialia, vol. 68, no. 6, pp. 384–388, 2013.
- [32] Z. K. Teng, C. T. Liu, G. Ghosh, P. K. Liaw, and M. E. Fine, “Effects of Al on the microstructure and ductility of NiAl-strengthened ferritic steels at room temperature,” Intermetallics, vol. 18, no. 8, pp. 1437–1443, Aug. 2010.
- [33] F. Qian, J. Sharp, and W. M. Rainforth, “Characterisation of L21-ordered Ni₂TiAl precipitates in FeMn maraging steels,” Materials Characterization, vol. 118, pp. 199–205, 2016.
- [34] J. Millán, S. Sandlöbes, A. Al-Zubi, T. Hickel, P. Choi, J. Neugebauer, D. Ponge, and D. Raabe, “Designing Heusler nanoprecipitates by elastic misfit stabilization in Fe–Mn maraging steels,” Acta Materialia, vol. 76, pp. 94–105, Sep. 2014.
- [35] Z. Zhang, C. T. Liu, M. K. Miller, X.-L. Wang, Y. Wen, T. Fujita, A. Hirata, M. Chen, G. Chen, and B. A. Chin, “A nanoscale co-precipitation approach for property enhancement of Fe-base alloys,” Scientific reports, vol. 3, p. 1327, Jan. 2013.
- [36] J. Tiley, G. B. Viswanathan, R. Srinivasan, R. Banerjee, D. M. Dimiduk, and H. L. Fraser, “Coarsening kinetics of γ' precipitates in the commercial nickel base Superalloy René 88 DT,” Acta Materialia, vol. 57, no. 8, pp. 2538–2549, May 2009.
- [37] M. F. Ashby and L. M. Brown, “Diffraction contrast from spherically symmetrical coherency strains,” Philosophical Magazine, vol. 8, no. 91, pp. 1083–1103, Jul. 1963.
- [38] D. Duchateau and M. Guttmann, “An X-ray microanalysis study of the partition of manganese in 6 and 9% Mn cryogenic steels and its influence on the stability of austenite dispersed in a tempered martensitic matrix,” Acta Metallurgica, vol. 29, no. 7, pp. 1291–1297, Jul. 1981.
- [39] J. Martínez, S. M. Cotes, A. F. Cabrera, J. Desimoni, and A. Fernández Guillermot, “On the relative fraction of ϵ martensite in γ -Fe–Mn alloys,” Materials Science and Engineering: A, vol. 408, no. 1–2, pp. 26–32, 2005.
- [40] R. W. K. Honeycombe and H. K. D. H. Bhadeshia, Steels: Microstructure and Properties. Oxford: Butterworth-Heinemann, 2006.
- [41] K. Detert, “No Title,” Trans. ASM, p. 262, 1966.
- [42] G. . Ansell and F. . Lenel, “Criteria for yielding of dispersion-strengthened alloys,” Acta Metallurgica, vol. 8, no. 9, pp. 612–616, Sep. 1960.
- [43] G. S. Ansell, “Fine particle effect in dispersion-strengthening,” Acta Metallurgica, vol.

- [44] E. V Pereloma, A. Shekhter, M. K. Miller, and S. P. Ringer, “Ageing behaviour of an Fe–20Ni–1.8Mn–1.6Ti–0.59Al (wt%) maraging alloy: clustering, precipitation and hardening,” *Acta Materialia*, vol. 52, no. 19, pp. 5589–5602, 2004.
- [45] V. K. Vasudevan, S. J. Kim, and C. M. Wayman, “Precipitation reactions and strengthening behavior in 18 Wt Pct nickel maraging steels,” *Metallurgical Transactions A*, vol. 21, no. 10, pp. 2655–2668, Oct. 1990.
- [46] P. J. Jacques, F. Delannay, and J. Ladrière, “On the influence of interactions between phases on the mechanical stability of retained austenite in transformation-induced plasticity multiphase steels,” *Metallurgical and Materials Transactions A*, vol. 32, no. 11, pp. 2759–2768, Nov. 2001.
- [47] E. Jimenez-Melero, N. H. van Dijk, L. Zhao, J. Sietsma, S. E. Offerman, J. P. Wright, and S. van der Zwaag, “Martensitic transformation of individual grains in low-alloyed TRIP steels,” *Scripta Materialia*, vol. 56, no. 5, pp. 421–424, Mar. 2007.
- [48] H. YANG and H. BHADESHIA, “Austenite grain size and the martensite-start temperature,” *Scripta Materialia*, vol. 60, no. 7, pp. 493–495, Apr. 2009.
- [49] P. Wang, N. Xiao, S. Lu, D. Li, and Y. Li, “Investigation of the mechanical stability of reversed austenite in 13%Cr–4%Ni martensitic stainless steel during the uniaxial tensile test,” *Materials Science and Engineering: A*, vol. 586, pp. 292–300, Dec. 2013.
- [50] M.-M. Wang, C. C. Tasan, D. Ponge, A. Kostka, and D. Raabe, “Smaller is less stable: Size effects on twinning vs. transformation of reverted austenite in TRIP-maraging steels,” *Acta Materialia*, vol. 79, pp. 268–281, Oct. 2014.
- [51] X. C. Xiong, B. Chen, M. X. Huang, J. F. Wang, and L. Wang, “The effect of morphology on the stability of retained austenite in a quenched and partitioned steel,” *Scripta Materialia*, vol. 68, no. 5, pp. 321–324, Mar. 2013.
- [52] I. B. Timokhina, P. D. Hodgson, and E. V. Pereloma, “Effect of microstructure on the stability of retained austenite in transformation-induced-plasticity steels,” *Metallurgical and Materials Transactions A*, vol. 35, no. 8, pp. 2331–2341, Aug. 2004.
- [53] S. Zhang and K. O. Findley, “Quantitative assessment of the effects of microstructure on the stability of retained austenite in TRIP steels,” *Acta Materialia*, vol. 61, no. 6, pp. 1895–1903, Apr. 2013.
- [54] L. T. Shiang and C. M. Wayman, “Maraging behavior of an Fe-19.5Ni-5Mn alloy II: Evolution of reverse-transformed austenite during overaging,” *Metallography*, vol. 21, no. 4, pp. 425–451, 1988.
- [55] D. Raabe, S. Sandlöbes, J. Millán, D. Ponge, H. Assadi, M. Herbig, and P.-P. Choi, “Segregation engineering enables nanoscale martensite to austenite phase transformation at grain boundaries: A pathway to ductile martensite,” *Acta Materialia*, vol. 61, no. 16, pp. 6132–6152, Sep. 2013.
- [56] F. Qian, “Microstructural evolution of Mn-based maraging steels and their influences on mechanical properties,” The University of Sheffield, 2015.
- [57] H. Huang, O. Matsumura, and T. Furukawa, “Retained austenite in low carbon, manganese steel after intercritical heat treatment,” *Materials Science and Technology*, vol. 10, no. 7, p. 621, Jul. 1994.